Engineering Reports

WILEY

Engineering Reports Open Access

RESEARCH ARTICLE OPEN ACCESS

Design of Two-Segment Constant-Force Compliant Mechanisms via Stiffness-Matched Parallel Integration

Junfeng Hu | Xiwei Jiang

School of Mechanical & Electrical Engineering, Jiangxi University of Science and Technology, Ganzhou, China

Correspondence: Junfeng Hu (hjfsuper@126.com)

Received: 4 February 2026 | **Revised:** 20 April 2026 | **Accepted:** 24 April 2026

Keywords: compliant mechanism | constant-force compliant mechanism | negative stiffness | two-segment constant force region | zero stiffness

ABSTRACT

This study presents a well-defined design paradigm for multi-segment constant-force compliant mechanisms (CFCMs). These CFCMs are capable of achieving dual-stage zero-stiffness characteristics via innovative stiffness hybridization. To tackle the critical limitation of conventional single-range constant-force mechanisms, we put forward two distinct configurations: a discrete two-state CFCM equipped with reconfigurable stiffness modules, and a continuous dual-stage architecture that employs cascaded negative stiffness elements. The core innovation is centered on the synergistic integration of positive-stiffness structures with hierarchical negative-stiffness mechanisms, namely bistable beams and their compensated derivatives, to establish overlapping zero-stiffness regimes. By means of analytical modeling using elliptic integrals and pseudo-rigid-body approximations, combined with finite element validation, we illustrate that the mechanisms can sustain constant forces of 4 N (1.2–5.6 mm) and 20 N (12.2–15.1 mm) within continuous motion trajectories. Experimental characterization of 3D-printed prototypes confirms that the force variation is less than 5% across the designated displacement ranges, and it attains an extension of the operational range in comparison with single-stage counterparts. This stiffness engineering framework offers multi-phase force regulation capabilities for applications that demand adaptive interaction forces, spanning from precision microassembly to bio-compatible robotic manipulation.

1 | Introduction

The constant-force compliant mechanism (CFCM) delivers a nearly invariant output force over a defined deformation range—hence its alternative designation as a zero-stiffness mechanism [1–5]. This distinctive mechanical behavior underpins broad applicability across engineering domains, including precision manipulation, biomedical instrumentation, and micro/nano-scale operations [3–9]. In robotic fruit harvesting, for instance, CFCMs mitigate tissue bruising by eliminating force overshoot during clamping [2]; in microgripping, their consistent force output prevents damage to fragile specimens caused by uncontrolled gripping forces [4–6]. Moreover, the intrinsic capacity to sustain near-constant force renders CFCMs highly effective in passive vibration isolation and impact buffering systems [5, 10].

Active control strategies can modulate the force–displacement response to emulate constant-force behavior [7]. Yet such approaches mandate real-time sensing (e.g., force and displacement feedback) and dedicated closed-loop controllers—introducing structural complexity, calibration overhead, and elevated cost. Crucially, robust force regulation remains challenging when interacting with unstructured or uncertain environments [11–13]. Alternatively, passive stiffness-tuning via discrete elastic elements (e.g., springs) has been explored to realize constant-force characteristics [8, 14]. However, this method suffers from inherent limitations in high-precision

contexts—including backlash, Coulomb friction, and progressive wear—compromising repeatability and long-term stability.

Compliant mechanisms offer a compelling alternative: they transmit motion and load solely through controlled elastic deformation, thereby eliminating joints, friction, wear, and assembly clearances while enabling monolithic fabrication and sub-micron positioning accuracy [9, 15–20]. Their suitability for constant-force design stems from two complementary stiffness regimes: (i) positive stiffness under initial loading, and (ii) negative stiffness induced by post-buckling deformation beyond the critical Euler load. By strategically integrating these opposing stiffness contributions—typically through parallel or hybrid configurations—a net near-zero stiffness (i.e., constant-force) response can be achieved over a prescribed load range [18, 19, 21]. Critically, this passive architecture obviates the need for sensors or active control, enhancing reliability and scalability.

Two principal paradigms govern CFCM design. The first relies on structural optimization—either distributed shape optimization or topology optimization—to directly synthesize zero-stiffness behavior [18–20, 22, 23]. While powerful, shape optimization entails high computational expense and parametric sensitivity; topology-optimized designs often yield geometrically complex, non-manufacturable layouts [24–26]. These limitations motivate alternative paradigms like stiffness antagonism for more tractable, manufacturable CFCM design. The second paradigm exploits stiffness antagonism: deliberately coupling positive- and negative-stiffness substructures (e.g., pre-buckled beams with linear springs) to cancel net stiffness over a target displacement interval [19, 21]. Zero stiffness here denotes a region wherein the derivative of force with respect to displacement $dF/d\delta \approx 0$—achievable, for example, by paralleling a positive-stiffness element with a negative-stiffness element whose force–displacement slope is equal in magnitude but opposite in sign.

Illustrative implementations include bistable-beam-based gripper, which achieves invariant clamping force without external actuation or sensing [19]; a magnetically coupled scanning probe that maintains consistent tip–sample interaction force via integrated negative-stiffness guidance [27]; and an Euler-buckled beam-spring shock absorber engineered for low-frequency vibration suppression [28]. A torsion shock suppressor—combining a pre-compressed cam-roller mechanism with positive torsional stiffness—has also been proposed for rotational vibration isolation [10]. Nevertheless, all existing CFCMs exhibit only a single constant-force stroke [4, 29, 30], whereas practical applications (e.g., multi-stage robotic manipulation, adaptive prosthetics, or graded tissue interaction) demand multi-section constant-force profiles—that is, distinct, controllable force plateaus across sequential displacement intervals. To address this gap, this paper introduces three novel design concepts enabling compliant mechanisms with two-section constant-force ranges.

Specifically, Section 2 presents a discrete CFCM generating two independent, fixed-force plateaus; Section 4 details a continuous two-segment CFM exhibiting smooth transitions between two distinct constant-force regimes. Concluding remarks, including limitations and future directions, are provided in Section 4.

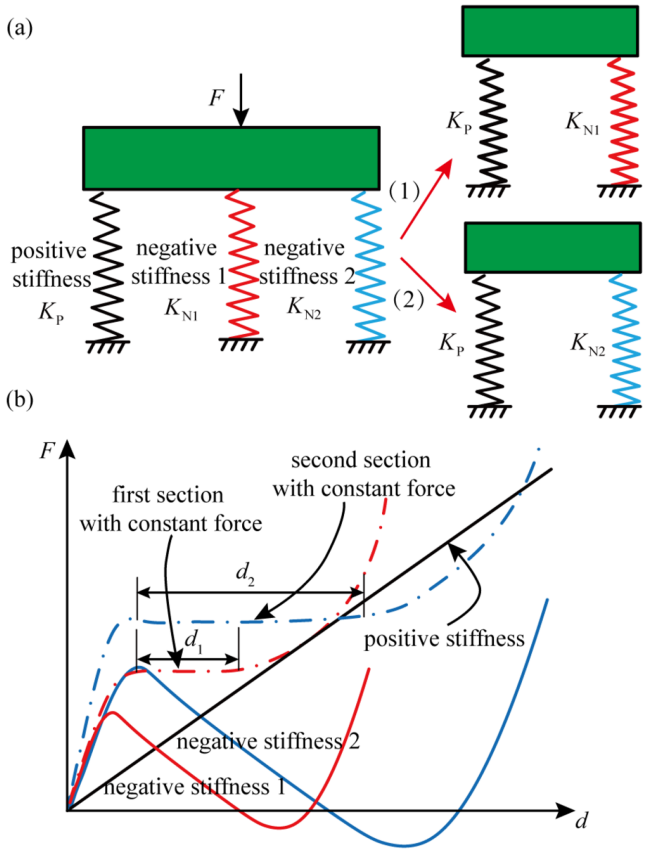

FIGURE 1 | Design idea of non-adjustable CFM. (a) Design schema. (b) Diagram of the mechanical relationship of the CFM.

2 | Design of Discrete CFM

2.1 | Design Idea

The design concept of the two-section constant-force mechanism is illustrated in Figure 1a, wherein two negative-stiffness substructures are arranged in parallel with a single positive-stiffness element. To realize two distinct zero-stiffness ranges—that is, two sequential intervals over which $dF/d\delta = 0$—the two negative-stiffness substructures share identical negative stiffness magnitudes but are deliberately designed to activate over non-overlapping, staggered displacement intervals. Specifically, their negative-stiffness behaviors initiate and terminate at different deformation thresholds, thereby enabling sequential stiffness cancellation. As a result, when integrated with a base positive-stiffness compliant structure, the composite system exhibits two consecutive plateaus of near-constant force output, each corresponding to the active engagement of one negative-stiffness substructure.

The design principle of the discrete CFCM is illustrated in Figure 1b. A single positive-stiffness mechanism (PSM) with a linear force–displacement response is selectively coupled—via mechanical switching—with two distinct negative-stiffness mechanisms (NSMs), each tuned to cancel the PSM's stiffness over a separate displacement interval. This architecture yields a two-segment constant-force output: in State I, the PSM operates in parallel exclusively with NSM-1, whose negative stiffness magnitude exactly offsets that of the PSM, thereby establishing

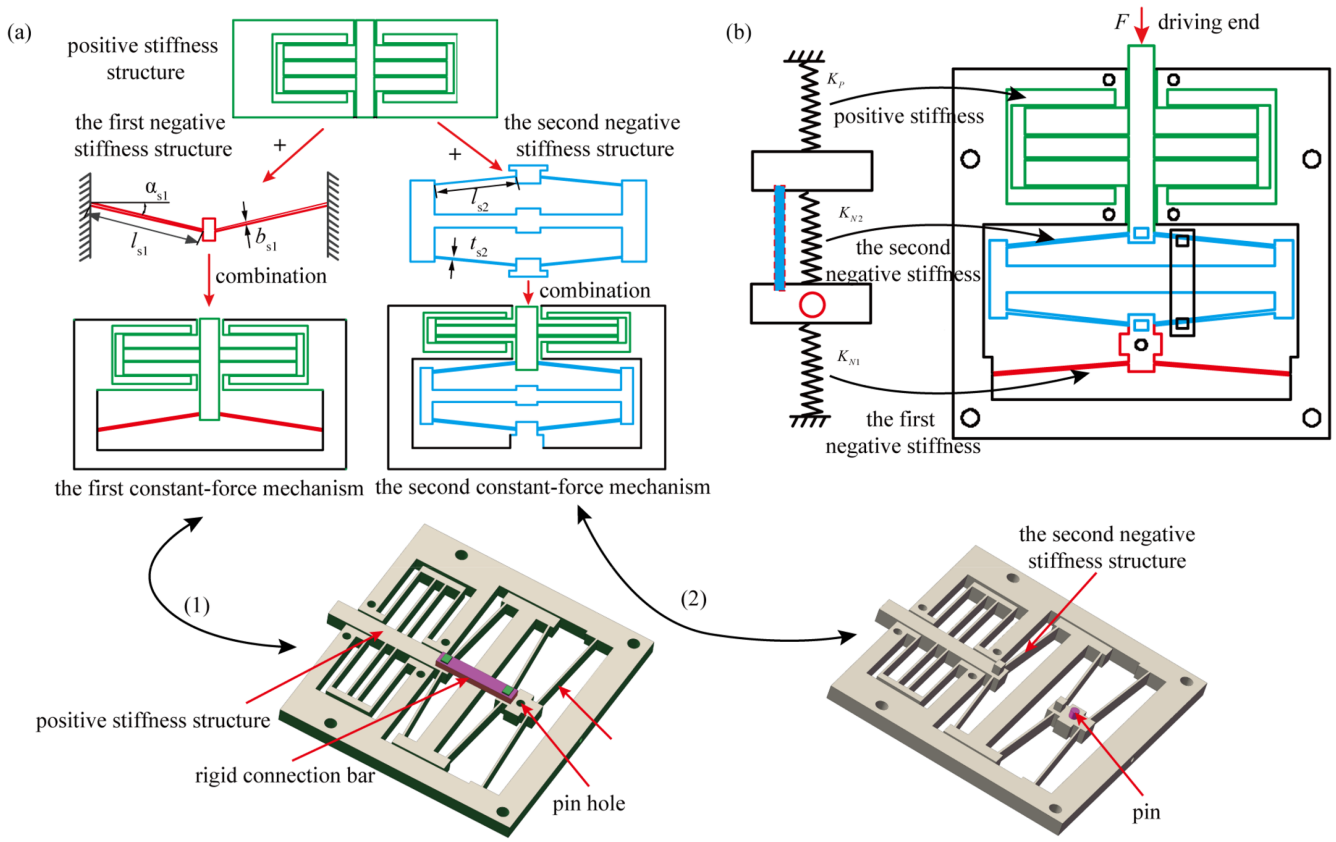

FIGURE 2 | Design of non-adjustable CFM. (a) Structural design. (b) State transmission.

the first zero-stiffness region as shown in Figure 1a; in State II, the switching element reconfigures the load path so that the PSM engages solely with NSM-2—identical in stiffness magnitude to NSM-1 but activated at a higher deformation threshold—producing a second, non-overlapping zero-stiffness region. The transition between states is achieved through a deterministic, repeatable mechanical switch (e.g., a cam-actuated latch or bistable toggle), ensuring reliable and hysteresis-free state selection. Thus, this discrete switching strategy enables robust realization of a dual-section constant-force compliant mechanism.

2.2 | Structural Design

The positive-stiffness mechanism (PSM) is implemented using a monolithic combined beam that exhibits a linear force-displacement response within its operational range. The first negative-stiffness mechanism (NSM-1) is realized as a single bistable beam, while the second negative-stiffness mechanism (NSM-2)—engineered to deliver an identical negative stiffness magnitude but over a shifted displacement interval—is configured as two identical bistable beams connected in series. This series arrangement increases the overall deformation threshold required to activate buckling, thereby delaying NSM-2's engagement relative to NSM-1. Two critical design considerations govern the system: (i) precise stiffness matching—ensuring the absolute value of each NSM's negative stiffness equals that of the PSM to guarantee complete stiffness cancellation in each state; and (ii) deterministic mechanical transition—designing the switching interface to enable unambiguous, repeatable, and backlash-free reconfiguration between the two parallel coupling modes.

Figure 2a presents the structural layout of the discrete CFCM. The first constant-force region is established by mechanically coupling the positive-stiffness module (PSM) in parallel with the first negative-stiffness module (NSM-1). A rigid transition bar serves a dual function: it directly transmits load between the PSM and NSM-1, while simultaneously decoupling the PSM from NSM-2—thereby constraining NSM-2 to remain undeformed and inactive throughout the first state.

The second constant-force region is activated via a deterministic mechanical reconfiguration: a removable pin is inserted into a dedicated pinhole located at the proximal end of NSM-1. This action rigidly fixes NSM-1's front end, suppressing its buckling deformation and effectively disabling it. Concurrently, removal of the rigid transition bar (or its disengagement via the pin insertion) enables direct parallel coupling between the PSM and NSM-2. As a result, the system transitions to State II, wherein NSM-2—tuned to the same negative stiffness magnitude as NSM-1 but with a higher activation threshold—engages with the PSM to produce the second zero-stiffness region. This binary, switch-driven architecture ensures unambiguous, repeatable, and hysteresis-minimized state transitions between two distinct constant-force plateaus.

2.3 | Stiffness Matching

Stiffness matching between the positive- and negative-stiffness substructures is systematically analyzed to ensure exact cancellation in each operational state. The bistable beam—selected as the negative-stiffness element—exhibits a well-documented post-buckling response that generates a controllable negative stiffness region [30, 31]. Its force–displacement characteristic, derived analytically via the elliptic integral method, quantitatively defines both the magnitude and displacement bounds of this negative stiffness. As shown in Figure 3a, the bistable beam consists of two identical slender beams clamped at one end and connected by a rigid central link; under axial compression, it undergoes symmetric snap-through buckling, producing a distinct softening branch in the load-deflection curve where $dF/d\delta < 0$. This nonlinear behavior is rigorously modeled using elliptic integrals to capture geometric nonlinearity and large deflections—enabling accurate prediction of the critical buckling load, negative stiffness slope, and stable deformation range.

$$F_s = 2(P\cos\varphi\sin\alpha - P\sin\varphi\cos\alpha) \tag{1}$$

where P is the mutual force between the sliding block and beam, α and φ represents the angles between F_s and y-axis, P and the x-axis, respectively.

Since the bistable beam is symmetrical, we select its left half as the analyzed object, as shown in Figure 3b.

$$\frac{b}{L} = -\frac{1}{\sqrt{\lambda}}\begin{pmatrix}\sin\varphi(2E(\kappa,\phi_2) - 2E(\kappa,\phi_1) + F(\kappa,\phi_1)\\ -F(\kappa,\phi_2) + 2\kappa\cos\varphi(\cos\phi_1 - \cos\phi_2)\end{pmatrix} \tag{2}$$

$$\frac{a}{L} = -\frac{1}{\sqrt{\lambda}}\begin{pmatrix}\cos\varphi(2E(\kappa,\phi_2) - 2E(\kappa,\phi_1) + F(\kappa,\phi_1) -\\ F(\kappa,\phi_2) + 2\kappa\sin\varphi(\cos\phi_2 - \cos\phi_1)\end{pmatrix} \tag{3}$$

where is the 2nd incomplete elliptic integral? It can be written as follows:

$$E(\kappa,\phi) = \int_0^{\phi}\sqrt{1-\kappa^2\sin^2\delta}\,d\delta \tag{4}$$

According to Equations (2–4), the vertical displacement b and horizontal displacement a of the beam end can be determined when the parameters κ, ϕ_1 and ϕ_2 are determined.

For the fixed guide beam structure, the variables ϕ_1 ϕ_2 satisfy the following relationship.

$$\sin\phi_1 = \frac{1}{\kappa}\cos\left(\frac{\varphi}{2}\right)$$
$$\sin\phi_2 = \sin\phi_1 \tag{5}$$

To determine the stiffness of the beam, we calculate the force F when the displacement d of the slider is specified. However, this relationship cannot be directly derived from the aforementioned formula and must instead be obtained through an iterative method. The iteration process can be described as follows:

1. When the displacement of the slider is d, the horizontal and vertical deformation of the beam can be obtained as follows:

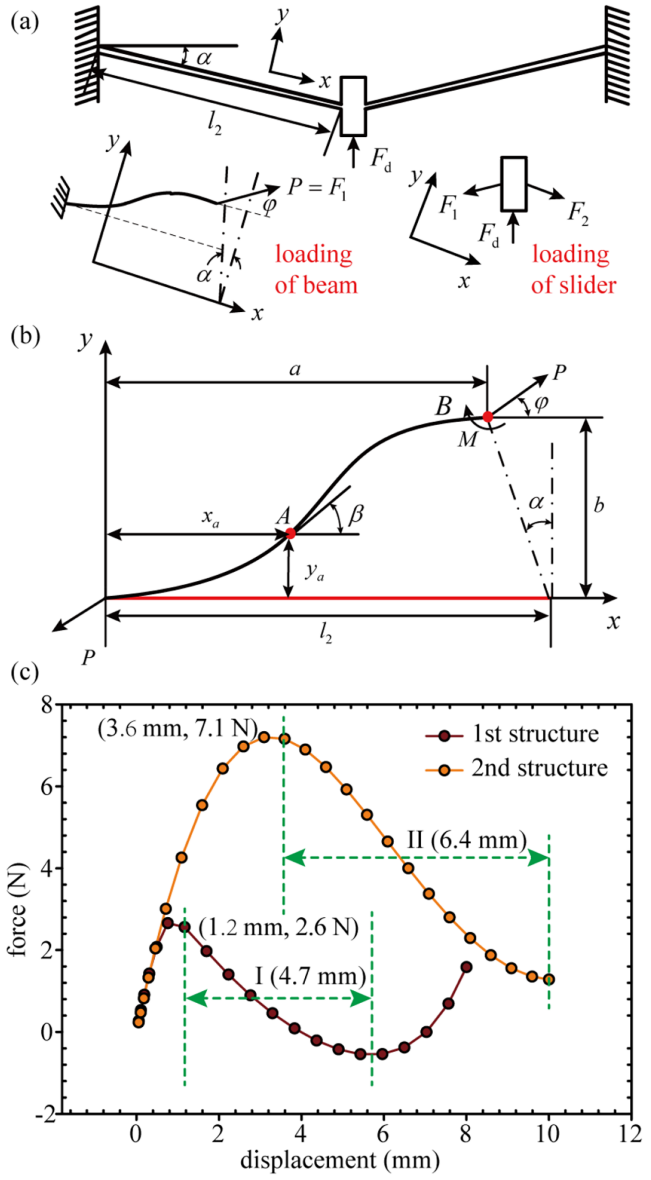

FIGURE 3 | Negative stiffness mechanism and its mechanical performance. (a) Bistable beam structure. (b) Force-displacement curve of the two negative stiffness structures. (c) The load-deflection curves of NSM-1 and NSM-2.

$$a_0 = l_2 - d\sin\alpha$$
$$b_0 = d\cos\alpha \tag{6}$$

2. As the parameters κ, φ are set as initial values, the ϕ_1 and ϕ_2 can be calculated by Equation (5). The force F_s corresponding to the displacement d can be calculated from these parameters. The displacement a and b can also be obtained. These displacements compare with the target values a_0 and b_0, and continue iterating if they are not equal; if equal, the resulting force corresponding to expected displacements can be obtained.

The second negative-stiffness module (NSM-2) comprises two identical bistable beams arranged in parallel—doubling the axial load capacity while preserving the negative stiffness slope per unit width. Its mechanical behavior is modeled using the

same elliptic integral framework applied to NSM-1, ensuring consistency in analytical treatment and enabling direct quantitative comparison. As shown in Figure 3c, the load-deflection curves of NSM-1 and NSM-2 reveal two key design-differentiating features:

1. Activation threshold offset: NSM-2 initiates its negative-stiffness regime at a significantly higher displacement (3.6 mm vs. 1.2 mm) and axial force (7.1 N vs. 2.6 N), reflecting its deliberately increased structural stability—achieved through the parallel configuration's enhanced buckling resistance. This staggered activation enables sequential engagement with the PSM, forming the foundation for two distinct constant-force plateaus.
2. Negative-stiffness range extension: NSM-2 exhibits a 2.3× wider negative-stiffness interval ($\Delta\delta = 1.8$ mm) compared to NSM-1 ($\Delta\delta = 0.78$ mm), while maintaining near-identical negative stiffness magnitude (−0.82 N/mm for NSM-2 vs. −0.85 N/mm for NSM-1). This extended operational window ensures robust force regulation over a larger deformation segment in State II.

The positive-stiffness module (PSM) consists of four symmetric flexure beams arranged in a cross configuration, as depicted in Figure 4a. To enable efficient and accurate stiffness matching, its quasi-static response is modeled using the pseudo-rigid-body method (PRBM). Exploiting structural symmetry, only one quadrant (beams AB and CD, plus the central rigid link) is modeled explicitly; the full system response is reconstructed via kinematic superposition. As illustrated in Figure 4b, each flexure beam is represented by a rigid segment connected to its neighbor through an ideal torsional spring, whose stiffness is calibrated against finite-element benchmarks to ensure sub-3% error in predicted force–displacement linearity across the target range.

The stiffness of the beam that is equivalent to a torsional spring is [32].

$$k_{Ti} = 2\lambda k_\theta \frac{EI}{l_i} \tag{7}$$

where λ is characteristic radius coefficient, k_θ is the stiffness coefficient of torsional spring, E is the elastic module of material, I is the inertia moment of beam section, l_i is the length of the beam.

The force P is represented by a vector.

$$\vec{P} = P\hat{i} \tag{8}$$

The force is rewritten

$$\vec{Z} = \left(R_1 \sin\theta_1 + m + R_2 \sin\theta_2\right)\hat{i} \tag{9}$$

where $R_i = \lambda l_{di}$, θ_i is the angle between the pseudo rigid bar and the x-axis.

The θ_1 is selected as generalized coordinates. By differentiating Equation (9) against the generalized coordinates θ, the virtual displacement of the slider can be obtained.

$$\delta\vec{Z} = \left(R_1 \cos\theta_1 + R_2 \cos\theta_2 \frac{d\theta_2}{d\theta_1}\right)\delta\theta_1 \tag{10}$$

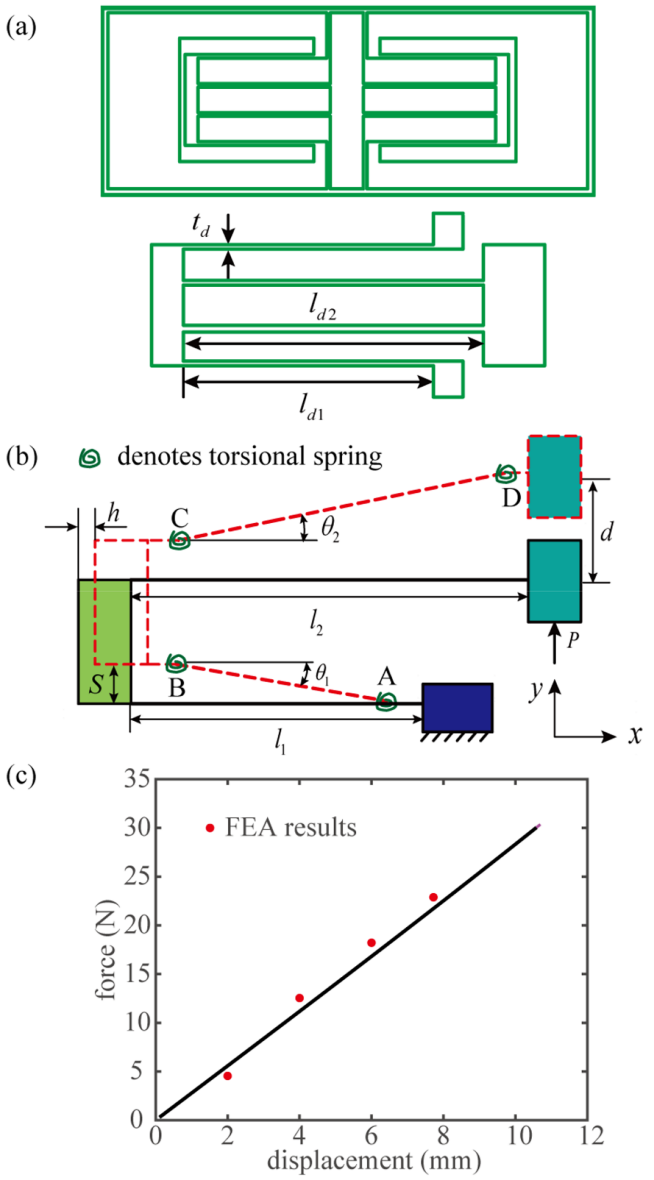

FIGURE 4 | Positive-stiffness compliant mechanism. (a) Structure. (b) Pseudo-rigid-body model. (c) Force-displacement relationship of the positive-stiffness structure.

The virtual work generated by the force P is

$$\delta W_F = P\left(R_1 \cos\theta_1 + R_2 \cos\theta_2 \frac{d\theta_2}{d\theta_1}\right)\delta\theta_1 \tag{11}$$

The virtual work from the deformation of the beam AB is

$$\delta W_{T1} = -2k_{t1}\theta_1\delta\theta_1 \tag{12}$$

The virtual work done by the beam CD is

$$\delta W_{T2} = -2k_{t2}\theta_2 \frac{d\theta_2}{d\theta_1}\delta\theta_1 \tag{13}$$

The virtual work of the mechanism is the sum of the above ones.

$$\delta W = \delta W_F + \delta W_{T1} + \delta W_{T_2} \tag{14}$$

The principle of virtual work is applied to obtain the following expression by substituting Equations (11–13) into (14).

$$P\left(R_1\cos\theta_1 + R_2\cos\theta_2\frac{d\theta_2}{d\theta_1}\right) - 2k_{t1}\theta_1 - 2k_{t2}\theta_2\frac{d\theta_2}{d\theta_1} = 0 \quad (15)$$

where

$$\frac{d\theta_2}{d\theta_1} = \frac{R_1\sin\theta_1}{R_2\sin\theta_2} \quad (16)$$

By substituting Equation (16) into Equation (15), the force P can be rewritten as follows:

$$P = \frac{2k_{t1}\theta_1 + 2k_{t2}\theta_2 R_1\sin\theta_1/R_2\sin\theta_2}{R_1\cos\theta_1 + R_1\sin\theta_1\cos\theta_2/\sin\theta_2} \quad (17)$$

Using the geometric relation, the displacement of the slider along the y-axis is

$$d = R_1\sin\theta_1 + R_2\sin\theta_2 \quad (18)$$

Accordingly, Equations (16–18) are integrated to formulate the complete analytical load–displacement relationship of the PSM. Its effective axial stiffness is analytically derived as $K_p = 2P/d$—where P denotes the applied compressive force and d represents the symmetric lateral deflection of the central node—confirming linear elastic behavior within the design range. The PRBM simplifies the complex compliant PSM by representing distributed flexure compliance as discrete torsional springs, reducing the system to a kinematically determinate rigid-link mechanism. This enables efficient closed-form force–displacement derivation via virtual work (Equations (11–18)). Prediction accuracy is validated against geometrically nonlinear FEA: the torsional spring stiffness is calibrated to minimize error, yielding sub-3% agreement in stiffness across the design range, as confirmed by the overlapping analytical and FEA curves in Figure 4c.

As shown in Figure 4c, the simulated and analytical force-displacement curves exhibit excellent agreement, validating the linearity assumption and confirming compliance with the fundamental requirement for constant-force mechanism design: a well-defined, predictable positive stiffness baseline.

The zero-stiffness matching protocol proceeds as follows: (i) The negative stiffness magnitude K_n of each NSM is extracted from its validated elliptic-integral-based model, ensuring fidelity to geometric nonlinearity and buckling physics; (ii) Per the stiffness cancellation principle, the target positive stiffness is set identically: $K_p = |K_n|$; (iii) PSM structural parameters including beam length, thickness, and width, are systematically optimized via parametric sweep to achieve $K_p = 0.85$ N/mm (for NSM-1 matching) and $K_p = 0.82$ N/mm (for NSM-2 matching), respectively, while maintaining monotonic linearity and avoiding premature yielding. This workflow yields the final dimensional specifications for both the PSM and NSMs. For the discrete CFCM, stiffness cancellation is enforced separately in each state via mechanical switching: State I (PSM + NSM-1): K_p is tuned to $|K_{n1}| = 0.85$ N/mm over $\delta \in [1.2, 5.0]$ mm. State II (PSM + NSM-2): K_p is adjusted to $|K_{n2}| = 0.82$ N/mm over $\delta \in [3.2, 10.5]$ mm. The transition bar and pin ensure only one NSM contributes negative stiffness at a time, maintaining precise cancellation within each plateau (Figure 5).

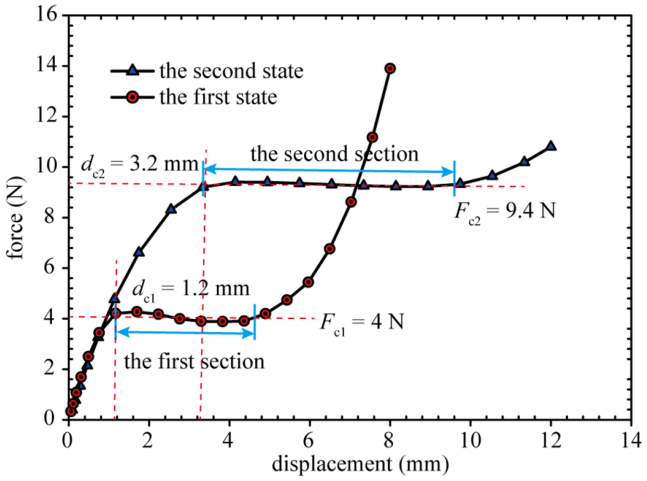

FIGURE 5 | Relationship between the force and displacement of the CFM.

Finite element analysis (FEA) was conducted to quantitatively evaluate the mechanical performance of the discrete CFCM under quasi-static loading. The finite element analysis employed a geometrically nonlinear quasi-static formulation suitable for large deflections and buckling. Solutions were obtained using an iterative Newton-type solver with automatic stabilization to handle potential instabilities in the post-buckling regime. Mesh refinement studies ensured solution convergence; element sizes were chosen to resolve beam bending and buckling modes adequately, and results were checked against analytical models for consistency.

The structure was modeled using isotropic PLA with an elastic modulus of 3.0 GPa and Poisson's ratio of 0.33, consistent with experimental material characterization. Two distinct operational configurations—State I (PSM‖NSM-1) and State II (PSM‖NSM-2)—were simulated under displacement-controlled compression. As shown in Figure 5, the FEA results confirm two well-defined constant-force plateaus: in State I, a near-constant output force of 4.0 N is sustained over the deformation interval [1.2–5.0] mm; in State II, a higher plateau of 9.4 N is maintained across [3.2–10.5] mm. Critically, both plateaus exhibit zero-stiffness behavior—thereby validating the two-segment constant-force design concept and its targeted force magnitudes.

3 | Design of Continuous Two-Segment CFM

The working principle of the continuous two-segment CFCM is based on the parallel integration of a linear Positive Stiffness Module (PSM) and a two-level Negative Stiffness Module (NSM). The total output force is the superposition of forces from both modules:

$$F_{\text{total}}(\delta) = F_p(\delta) + F_n(\delta) \quad (19)$$

where $F_p(\delta)$ is the force from the PSM, and $F_n(\delta)$ is the force from the NSM at displacement δ. The condition for achieving a constant-force (zero-stiffness) region is that the derivative of the total force with respect to displacement is zero:

$$\frac{dF_{\text{tatal}}}{d\delta} = K_p + K_n \approx 0 \quad (20)$$

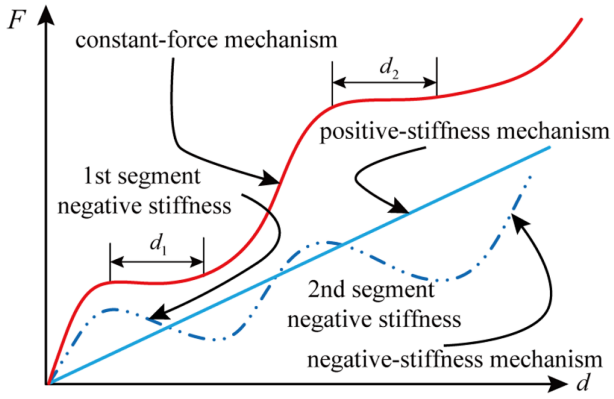

FIGURE 6 | Concept of continuous two-segment CFM.

Here, K_p is the constant positive stiffness of the PSM, and K_n is the negative stiffness of the NSM. The design goal is to engineer the NSM so that it exhibits two consecutive, non-overlapping displacement intervals where its negative stiffness is approximately constant and equal in magnitude to K_p, that is, $K_n \approx -K_p$, for $\delta \in [\delta_{a1}, \delta_{b1}]$ and $\delta \in [\delta_{a2}, \delta_{b2}]$.

The state transitions in the discrete CFCMs described previously rely on mechanical reconfiguration involving auxiliary components—resulting in inherently discontinuous force output between segments. To enable seamless, continuous-force regulation across two distinct plateaus within a single monotonic displacement sweep, we propose a continuous two-segment CFCM architecture, illustrated in Figure 6. Its design adheres to three rigorously defined conditions: (I) The negative-stiffness module (NSM) must generate two consecutive, non-overlapping negative-stiffness intervals in its native load–deflection response; (II) The magnitudes of negative stiffness in both intervals must be identical ($|K_{n1}| = |K_{n2}|$);(III) The positive-stiffness module (PSM) must exhibit a linear stiffness K_p precisely equal to this common negative-stiffness magnitude—ensuring complete $dF/d\delta \approx 0$ cancellation in both segments upon parallel integration.

To realize Condition (I), we synthesize a monolithic NSM by connecting NSM-1 and NSM-2 in series. As shown in Figure 7a, this arrangement sequences their buckling events: NSM-1 activates first, followed by NSM-2, yielding two adjacent negative-stiffness branches. FEA confirms this dual-branch behavior (Figure 7d). However, the raw slopes reveal a mismatch: $K_{n1} = -0.74$ N/mm and $K_{n2} = -1.02$ N/mm—violating Condition (II) by 38%. To rectify this, we redesign NSM-2 as a hybrid structure: a trapezoidal flexure beam—engineered to provide +0.34 N/mm positive stiffness—is integrated in parallel with the original bistable element (Figure 7b). This passive compensation scheme offsets the excess negative stiffness. Post-compensation FEA (Figure 7e) validates the correction, showing near-identical slopes (−0.68 N/mm vs. −0.74 N/mm) and contiguous zero-stiffness intervals. Finally, the PSM is parameterized to deliver $K_p = 0.71$ N/mm, satisfying Condition (III). The adjustment follows parallel stiffness superposition: $K_{n2,adj} = K_{n2,raw} + K_c$, where K_c is the compensation flexure's stiffness. With, $K_c \approx 0.34$ N/mm, matching $K_{n1} \approx -0.74$ N/mm and satisfying Condition (II). Thus, the series connection of NSM-1 and NSM-2 sequences their buckling events to produce two consecutive negative-stiffness intervals, while the parallel trapezoidal flexure passively compensates NSM-2's slope to match NSM-1's magnitude, enabling uniform cancellation with the PSM's K_p in both regions (Figure 7e).

The continuous two-segment CFM is realized by integrating the linear positive-stiffness module (PSM)—comprising four parallel flexure beams—with the compensated two-level negative-stiffness module (NSM) described in Section 4, as shown in Figure 8a. To experimentally validate the design, a monolithic prototype was fabricated from PLA via fused deposition modeling (FDM). The monolithic prototypes were fabricated from PLA material using 3D printing with standard process parameters to validate the design concept. The experimental setup (Figure 8b) employs a voice-coil actuator for displacement-controlled loading, a calibrated grating displacement sensor, and a precision force transducer (model: Kistler 9217A). Raw force and displacement signals were sampled synchronously at 1 kHz. Data were filtered with a 10 Hz low-pass moving average to attenuate high-frequency noise while preserving quasi-static trends. For each constant-force region, three repeated loading cycles were averaged to compute mean force ± standard deviation; the reported force variation (< 5%) is the maximum relative standard deviation across each plateau's displacement range.

Experimental results show excellent agreement with FEA predictions. Two distinct zero-stiffness regions—defined as intervals—are consistently observed: Region I spans [1.2–5.6] mm with a mean output force of 4.0 N; Region II extends over [12.2–15.1] mm at 20.0 N. Critically, the transition between regions occurs smoothly without force discontinuity or snap-through instability, confirming the efficacy of the series-connected, stiffness-compensated NSM architecture. These results conclusively demonstrate that parallel integration of a matched PSM and a two-level NSM enables robust realization of a continuous two-segment constant-force mechanism.

The stability of the designed constant-force compliant mechanism (CFCM) is fundamentally rooted in exploiting the buckling stability of bistable beams to create a controllable negative stiffness region, which, when paralleled with positive stiffness, yields zero stiffness. From a structural mechanics perspective, this zero-stiffness characteristic corresponds to a plateau in the system's total potential energy function, indicating a state of neutral equilibrium.

For a conservative system, the stability of an equilibrium is determined by the second derivative of the total potential energy, $\prod_{total}$, with respect to the generalized displacement, δ: if $\partial^2 \prod_{total} / \partial \delta^2 > 0$, the equilibrium is stable (positive stiffness); if < 0, it is unstable (negative stiffness); and if ≈ 0, it is neutrally stable (zero stiffness). In our mechanism, $\prod_{total}(\delta)$ is the sum of the potential energies of the positive stiffness module (PSM) and the negative stiffness module (NSM): $\prod_{total}(\delta) = \prod_p(\delta) + \prod_n(\delta)$. The output force is $F = -\partial \prod_{total} / \partial \delta$, and the effective stiffness is $K = \partial^2 \prod_{total} / \partial \delta^2$.

4 | Conclusions

This paper presents a framework for designing two-segment constant-force compliant mechanisms (CFCMs) through

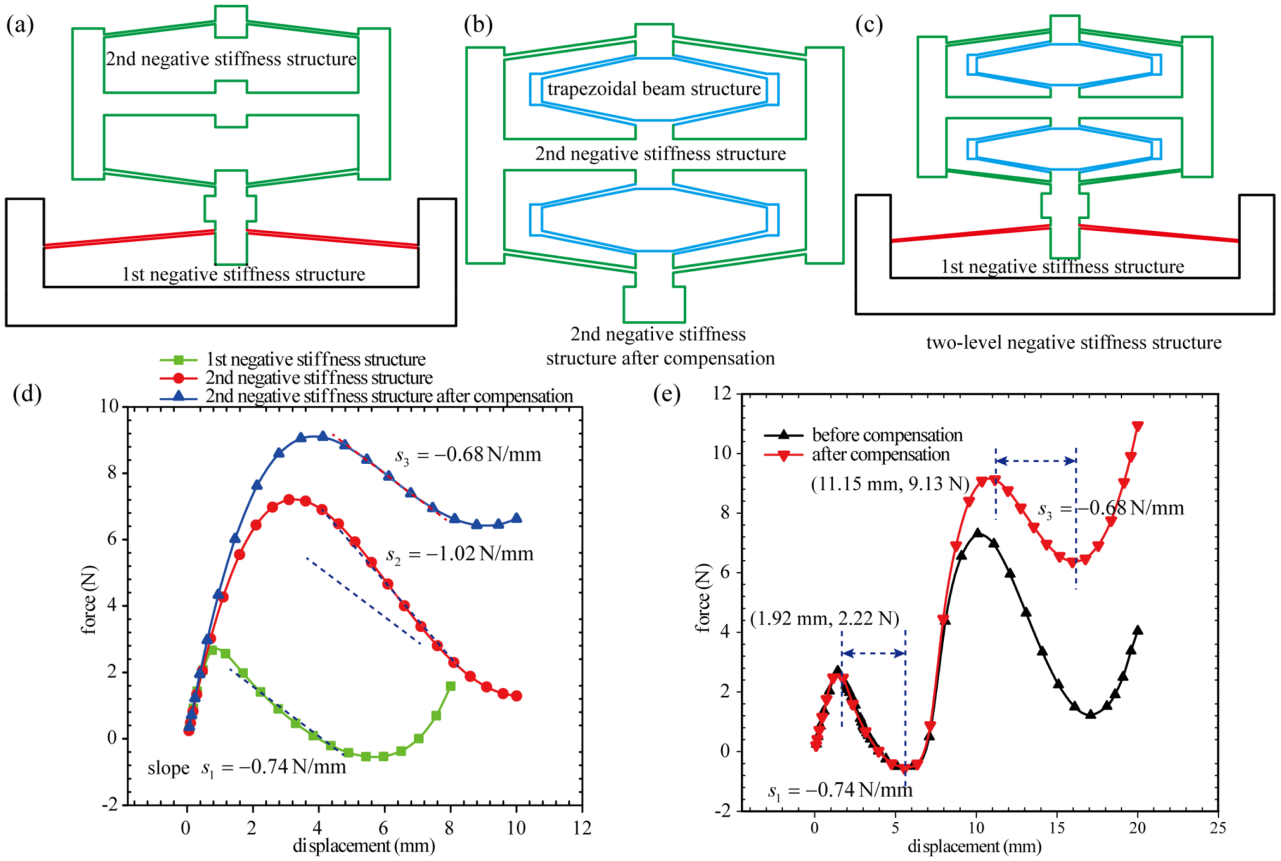

FIGURE 7 | Design of negative-stiffness compliant mechanism with two-segment negative-stiffness regions. (a) Initial design concept. (b) 2nd negative stiffness structure after compensation. (c) Two-level negative stiffness structure. (d) Stiffness of three kinds of negative structure. (e) Force–displacement curve of two-level negative stiffness structure.

stiffness-domain synthesis. Two distinct architectural strategies are proposed and comparatively evaluated: (i) Discrete-switching CFCM: A mechanically reconfigurable architecture that toggles between two independent PSM–NSM pairs to generate two sequential zero-stiffness regions within a shared displacement range. While enabling distinct force plateaus, its state transitions necessitate auxiliary components. (ii) Continuous-integration CFCM: A monolithic, transition-free architecture integrating a linear PSM with a series-compensated two-level NSM—engineered to produce two consecutive, stiffness-matched negative-stiffness intervals. This design achieves seamless, continuous-force regulation without mechanical switching or external actuation.

Both FEA simulations and experimental validation confirm the feasibility of the design concepts. For practical deployment, optimal CFCM performance requires maximizing plateau width while constraining force ripple of nominal output. Future work will address these objectives through topology-optimized PSM/NSM co-design and nonlinear parameter sensitivity analysis. Additionally, the extension of this stiffness-synthesis paradigm to spatial (3D) compliant mechanisms—enabling multi-axis constant-force delivery—is identified as a critical next-step research direction.

The discrete CFCM's switching is validated here under quasi-static assumptions appropriate for slow reconfiguration. For applications requiring rapid switching, future work could extend the energy formulation to include kinetic energy and solve Lagrange's equations of motion, incorporating contact models for pin/interface dynamics. This would analyze transient forces and settling behavior while leveraging the static compliance models developed in this work. The present work validates the two-segment CFCM design under standard laboratory conditions. For deployment in applications with varying environmental conditions, future research should focus on environmental robustness. The insights gained would be integral to a reliability-based or robust design optimization framework, ensuring the constant-force performance is maintained against environmental fluctuations, thereby transitioning the design from a laboratory prototype to a field-ready component. Furthermore, advancing the practical deployment of passive CFCMs requires ensuring their performance robustness against real-world uncertainties. This aligns with the growing emphasis on reliability-based design and uncertainty quantification in precision mechanics. While Monte Carlo simulation is computationally expensive, recent progress in adaptive surrogate-model-based reliability analysis offers efficient alternatives. Methods such as active learning Kriging and enhanced simulation techniques coupled with machine learning enable accurate failure probability prediction and robust design optimization under variations in material properties, geometric tolerances, and loading conditions [33–36]. Integrating these advanced computational frameworks into the CFCM design process represents a key research direction to formally enhance

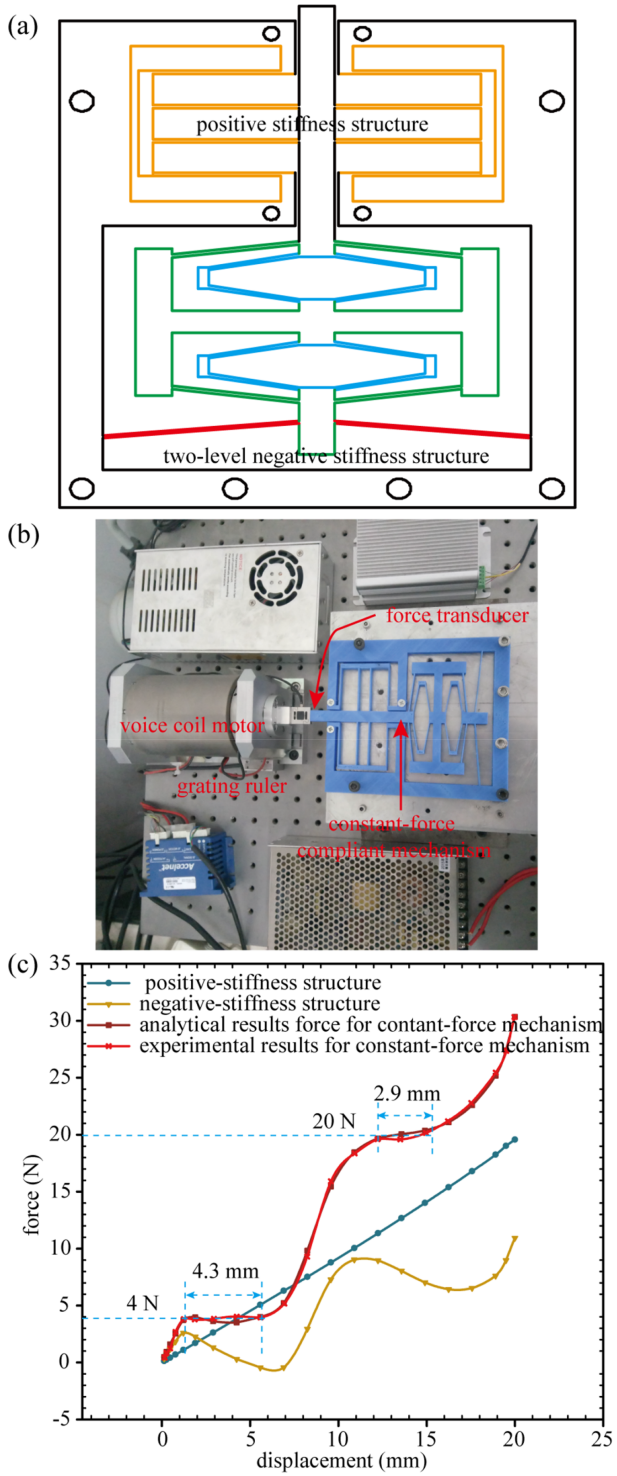

FIGURE 8 | Continuous CFM. (a) Structure of CFM. (b) Experimental set. (c) Force–displacement curve of the CFM.

the reliability and scalability of passive, sensor-free architectures like the one presented in this work.

Author Contributions

Junfeng Hu: conceptualization, methodology, funding acquisition, supervision, writing – original draft. **Xiwei Jiang:** data curation, investigation, formal analysis.

Acknowledgments

This work received funding from the National Natural Science Foundation of China (52165011), Science and technology plan project of Ganzhou (2023PGX16964).

Funding

This work was supported by the National Natural Science Foundation of China (52165011) and Science and technology plan project of Ganzhou (2023PGX16964).

Data Availability Statement

The data that support the findings of this study are available on request from the corresponding author. The data are not publicly available due to privacy or ethical restrictions.

Peer Review

For transparency, the peer review documents associated with this article are available at https://doi.org/10.1002/eng2.70811.

References

1. P. Wang and Q. Xu, "Design and Modeling of Constant-Force Mechanisms: A Survey," *Mechanism and Machine Theory* 119 (2018): 1–21.

2. J. Y. Wang and C. C. Lan, "A Constant-Force Compliant Gripper for Handling Objects of Various Sizes," *Journal of Mechanical Design* 136, no. 7 (2014): 1–10.

3. A. J. Lamers, J. A. G. Sánchez, and J. L. Herder, "Design of a Statically Balanced Fully Compliant Grasper," *Mechanism and Machine Theory* 92 (2015): 230–239.

4. H. T. Pham and D. A. Wang, "A Constant-Force Bistable Mechanism for Force Regulation and Overload Protection," *Mechanism and Machine Theory* 46, no. 7 (2011): 899–909.

5. A. Carrella, M. J. Brennan, and T. P. Waters, "Static Analysis of a Passive Vibration Isolator With Quasi-Zero-Stiffness Characteristic," *Journal of Sound and Vibration* 301, no. 5 (2007): 678–689.

6. Q. Xu, "Adaptive Discrete-Time Sliding Mode Impedance Control of a Piezoelectric Microgripper," *IEEE Transactions on Robotics* 29, no. 29 (2013): 663–673.

7. W. Zhang, A. Sobolevski, B. Li, Y. Rao, and X. Liu, "An Automated Force-Controlled Robotic Micromanipulation System for Mechanotransduction Studies of Drosophila Larvae," *IEEE Transactions on Automation Science and Engineering* 13, no. 2 (2016): 789–797.

8. R. Barents, M. Shenk, W. D. Dorsser, B. M. Wisse, and J. L. Herder, "Spring-To-Spring Balancing as Energy-Free Adjustment Method in Gravity Equilibrators," *Journal of Mechanical Design* 133, no. 6 (2011): 689–700.

9. P. Wang and Q. Xu, "Design and Testing of a Flexure-Based Constant-Force Stage for Biological Cell Micromanipulation," *IEEE Transactions on Automation Science and Engineering* 99 (2017): 1–13.

10. J. Zhou, D. Xu, and S. Bishop, "A torsion quasi-zero stiffness vibration isolator," *Journal of Sound and Vibration* 338 (2015): 121–133.

11. M. Debiao, Y. Shunqi, Z. Yu, and Z. Shunpeng, "Structural Reliability Analysis and Uncertainties-Based Collaborative Design and Optimization of Turbine Blades Using Surrogate Model," *Fatigue & Fracture of Engineering Materials & Structures* 42, no. 6 (2019): 1219–1227.

12. D. Meng, Z. Hu, J. Guo, Z. Lv, T. Xie, and Z. Wang, "An Uncertainty-Based Structural Design and Optimization Method With Interval Taylor Expansion," *Structure* 33 (2021): 4492–4500.

13. D. Meng, T. Xie, P. Wu, S.-p. Zhu, Z. Hu, and Y. Li, "Uncertainty-Based Design and Optimization Using First Order Saddle Point Approximation

Method for Multidisciplinary Engineering Systems," *ASCE-ASME Journal of Risk and Uncertainty in Engineering Systems* 6, no. 3 (2020): 1–10.

14. Y. Liu, D.-p. Yu, and J. Yao, "Design of an Adjustable Cam Based Constant Force Mechanism," *Mechanism and Machine Theory* 103 (2016): 85–97.

15. K. A. Tolman, E. G. Merriam, and L. L. Howell, "Compliant Constant-Force Linear-Motion Mechanism," *Mechanism and Machine Theory* 106 (2016): 68–79.

16. J. C. Meaders and C. A. Mattson, "Optimization of Near-Constant Force Springs Subject to Mating Uncertainty," *Structural and Multidisciplinary Optimization* 41, no. 1 (2010): 1–15.

17. C. V. Jutte and S. Kota, "Design of Nonlinear Springs for Prescribed Load-Displacement Functions," *Journal of Mechanical Design* 130, no. 8 (2008): 1188–1194.

18. P. Wang and Q. Xu, "Design of a Flexure-Based Constant-Force XY Precision Positioning Stage," *Mechanism and Machine Theory* 108 (2017): 1–13.

19. Y. Liu, Y. Zhang, and Q. Xu, "Design and Control of a Novel Compliant Constant-Force Gripper Based on Buckled Fixed-Guided Beams," *IEEE/ASME Transactions on Mechatronics* 22, no. 1 (2017): 476–486.

20. X. Zeng, C. Hurd, H.-J. Su, S. Song, and J. Wang, "A Parallel-Guided Compliant Mechanism With Variable Stiffness Based on Layer Jamming," *Mechanism and Machine Theory* 148 (2020): 103791.

21. Y.-H. Chen and C.-C. Lan, "Design of a Constant-Force Snap-Fit Mechanism for Minimal Mating Uncertainty," *Mechanism and Machine Theory* 55 (2012): 34–50.

22. T. Liu, S. Bi, Y. Yao, Z. Dong, Q. Yang, and L. Liu, "Research on Zero-Stiffness Flexure Hinge (ZSFH) Based on Spring Four-Bar Linkage (4BSL)," *Mechanism and Machine Theory* 143 (2020): 103633.

23. Y. Miao and J. Zheng, "Optimization Design of Compliant Constant-Force Mechanism for Apple Picking Actuator," *Computers and Electronics in Agriculture* 170 (2020): 105232.

24. H. Yang, S. Yang, D. Meng, et al., "Optimization of Analog Circuit Parameters Using Bidirectional Long Short-Term Memory Coupled With an Enhanced Whale Optimization Algorithm," *Mathematics* 13, no. 1 (2025): 121.

25. S. Yang, D. Meng, M. Alfouneh, B. Keshtegar, and S.-p. Zhu, "A Robust-Weighted Hybrid Nonlinear Regression for Reliability Based Topology Optimization With Multi-Source Uncertainties," *Computer Methods in Applied Mechanics and Engineering* 447 (2025): 118360.

26. M. Debiao, L. Yan, H. Chao, G. Jinbao, L. Zhiyuan, and W. Peng, "Multidisciplinary Design for Structural Integrity Using a Collaborative Optimization Method Based on Adaptive Surrogate Modelling," *Materials and Design* 206 (2021): 1–8.

27. H. Wang, J. Zhao, R. Gao, and Y. Yang, "A Novel Constant-Force Scanning Probe Incorporating Mechanical-Magnetic Coupled Structures," *Review of Scientific Instruments* 82 (2011): 075101.

28. X. Liu, X. Huang, and H. Hua, "On the Characteristics of a Quasi-Zero Stiffness Isolator Using Euler Buckled Beam as Negative Stiffness Corrector," *Journal of Sound and Vibration* 332 (2013): 3359–3376.

29. Y.-H. Chen and C.-C. Lan, "An Adjustable Constant-Force Mechanism for Adaptive End-Effector Operations," *Journal of Mechanical Design* 134 (2012): 31005.

30. G. L. Holst, G. H. Teichert, and B. D. Jensen, "Modeling and Experiments of Buckling Modes and Deflection of Fixed-Guided Beams in Compliant Mechanisms," *Journal of Mechanical Design* 133 (2011): 51002.

31. Z. Liu, F. Niu, H. Gao, et al., "Design, Analysis, and Experimental Validation of an Active Constant-Force System Based on a Low-Stiffness Mechanism," *Mechanism and Machine Theory* 130 (2018): 1–26.

32. J. Hu, T. Wen, and J. He, "Dynamics of Compliant Mechanisms Using Transfer Matrix Method," *International Journal of Precision Engineering and Manufacturing* 21 (2020): 2173–2189.

33. S. Yang, D. Meng, H. Wang, and C. Yang, "A Novel Learning Function for Adaptive Surrogate-Model-Based Reliability Evaluation," *Philosophical Transactions of the Royal Society A – Mathematical Physical and Engineering Sciences* 382, no. 2264 (2024): 20220395.

34. S. Yang, D. Meng, H. Yang, B. Keshtegar, A. M. P. de Jesus, and S.-p. Zhu, "Adaptive Kriging-Assisted Enhanced Sparrow Search With Augmented-Lagrangian First-Order Reliability Method for Highly Efficient Structural Reliability Analysis," *Reliability Engineering & System Safety* 267 (2026): 111916.

35. Y. Shiyuan, M. Debiao, Y. Hengfei, L. Changqi, and S. Xiaoyan, "Enhanced Soft Montecarlo Simulation Coupled With SVR for Structural Reliability Analysis," *Proceedings of the Institution of Civil Engineers Transport* 178, no. 7 (2025): 459–474.

36. S. Yang, D. Meng, H. Wang, Z. Chen, and B. Xu, "A Comparative Study for Adaptive Surrogate-Model-Based Reliability Evaluation Method of Automobile Components," *International Journal of Structural Integrity* 14, no. 3 (2023): 498–519.